

Research Paper**Finite Element Computations of Complex Flows**

SANJAY MITTAL*, GAURAV CHOPRA, M FURQUAN, NAVROSE, V M K KOTTEDA and VARUN BHATT

Department of Aerospace Engineering, Indian Institute of Technology Kanpur

(Received on 27 May 2016; Accepted on 29 May 2016)

A brief review of our research activities is presented. Stabilized finite element methods are used to solve two and three-dimensional, unsteady turbulent flows past complex bodies at various Reynolds (Re) and Mach (M) numbers. The stabilized finite element methods that are being used are robust, accurate and able to handle complex geometries including those that deform with time. Flow problems involving fluid-structure interactions as well as aerodynamic shape optimization for superior aerodynamic performance are also presented.

Keywords: FEM; Fluid Dynamics; Transition; Vortex Induced Vibrations; Fluid Structure Interaction; Shape Optimization

Introduction

The stabilized finite element formulation (Tezduyar et al., 1992) is utilized for simulating a large class of incompressible and compressible flow problems, including those with moving boundaries and interfaces. The stabilization is achieved by employing Streamline-Upwind/Petrov-Galerkin (SUPG) and Pressure-Stabilizing/Petrov-Galerkin (PSPG) methods (Tezduyar et al., 1992). The linear algebraic equations resulting from finite element discretization are solved using a matrix-free implementation of the GMRES technique (Saad and Schultz, 1986) with preconditioners.

The Parallel Implementation

The finite element formulation is implemented on a parallel computer (Behara and Mittal, 2009). The scalability of the implementation for up to 640 cores is evaluated for solutions on five finite element meshes with relatively large number of nodes and elements. The statistics for the meshes are presented in Table 1. The speed-up test was carried out on the HP-Proliant-SL-230s-Gen8 server: a high performance computing facility at the computer center, Indian Institute of Technology, Kanpur.

Table 1: Statistics (in millions) of various meshes used for testing speedup

mesh	Nodes	Elements	equations
M1	2.1	2.1	16.9
M2	8.5	8.4	67.4
M3	17.1	16.8	134.6
M4	34.1	33.6	269.1
M5	46.8	46.2	369.9

$$S = \frac{(T_{\min-procs})(n_{\min-procs})}{T_n} \quad (1)$$

Each node of this Linux cluster is based on an Intel Xeon E5-2670V with 2 CPU-Ivy Bridge that runs at a clock speed of 2.5 GHz. Each node has 20-cores and 128 GB of RAM. The interconnect is Infiniband that is capable of a throughput of up to 56Gbps. The peak performance of the machine with 900 compute nodes is: Rpeak=359.6 TFlops and Rmax=344.317 TFlops. The Speedup (S) is calculated using equation (1). Here $n_{\min-procs}$ is minimum number of processors on which the problem can be run, $T_{\min-procs}$ is time taken by problem on $n_{\min-procs}$, and T_n is

*Author for Correspondence: E-mail: smittal@iitk.ac.in

the time taken by the same problem on n processors. Figure 1 shows the variation of S with n . The scaling performance improves as one uses a more refined mesh. Mesh M5 is the most refined of all meshes. The flow solution on this mesh requires solving 369.9 million equations. As seen from Fig. 1, close to linear speedup is achieved on this mesh.

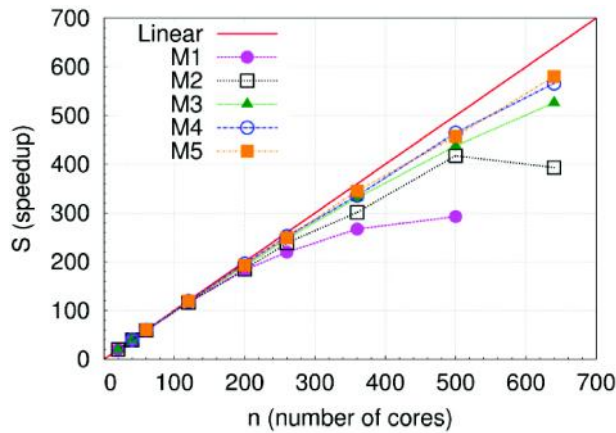


Fig. 1: Speedup of parallel finite element code on HPC 2013 machine

Drag Crisis in Flow Past a Circular Cylinder

Drag crisis is sudden drop in the drag experienced by a body as the Re is increased beyond a certain critical value. For a smooth circular cylinder, the critical Re at which drag crisis occurs is 2×10^5 , approximately. This phenomenon is associated with transition of boundary layer, from laminar to turbulent state. The turbulent boundary layer results in delay of flow separation over the surface of cylinder. This leads to increase in the base pressure and reduction in drag coefficient (\bar{C}_D). Roshko, 1961 categorized the flow past a smooth cylinder into four regimes: (i) subcritical: \bar{C}_D is constant with Re and its approximate value is 1.2, (ii) critical: the drag crisis occurs in this regime, (iii) supercritical: \bar{C}_D reduces to nearly 0.3 and, (iv) transcritical: \bar{C}_D increases gradually with Re to 0.7, approximately. The present work looks into predicting and understanding the mechanism of drag crisis in flow past a circular cylinder via 2D and 3D simulations. The 3D grid was prepared by stacking N_z number of 2D grid sections in spanwise direction. Bulk of the simulations were carried out without any turbulence

model. These are referred as model-free computations.

The variation of \bar{C}_D with Re is presented in Fig. 2. Also shown are the well established experimental and computational results. The present results are in reasonable agreement with data from earlier studies. Fig. 2 shows that both 2D and 3D model free simulations predict the drag crisis phenomenon at a slightly lower Re compared to experimental results. This figure also highlights that drag crisis phenomenon is predominantly 2D, as the critical regime lies in the same Re regime in both two and three dimensions. However, for subcritical and supercritical regime three dimensional simulations, with $N_z = 51$, provide a more accurate prediction of the values of \bar{C}_D . Figure 3 shows time and span averaged streamlines ($\bar{\Psi}$) and instantaneous spanwise vorticity (ω_z) at $Re = 5 \times 10^4$ and 3.5×10^5 . These lie in subcritical and supercritical regimes respectively. Fig. 3 explains the mechanism of transition of boundary layer from laminar to turbulent state. At $Re = 5 \times 10^4$ the boundary layer undergoes laminar separation. The separated shear layer becomes unstable at a downstream location. At higher Re , for example at $Re = 3.5 \times 10^5$ the separated shear layer reattaches to the surface and separates at a larger angle. The reattachment of the shear layer as a turbulent boundary layer is due to the enhanced mixing provided by the shear layer vortices which are created by the destabilization of the separated shear layer very near to the cylinder (Singh and Mittal, 2005). This mechanism also leads to the formation of Laminar Separation Bubble (LSB) on the surface of cylinder. LSB can be seen in the time- and span-averaged streamlines ($\bar{\Psi}$) of the $Re = 3.5 \times 10^5$ flow in Fig. 3(B). LSB is present on both the top and bottom surface of the cylinder, indicating that flow separation is symmetric. The delay in flow separation leads to narrower wake which causes the \bar{C}_D to reduce. This can be observed from figure 3 where $Re = 5 \times 10^4$ flow has a wider wake compared to 3.5×10^5 flow. Clearly the appearance of LSB is vital to the transition of boundary layer from a laminar to turbulent state. More importantly, it was also found that process of transition and appearance of LSB is an intermittent process in the critical regime where drag crisis occurs. This is quantified using

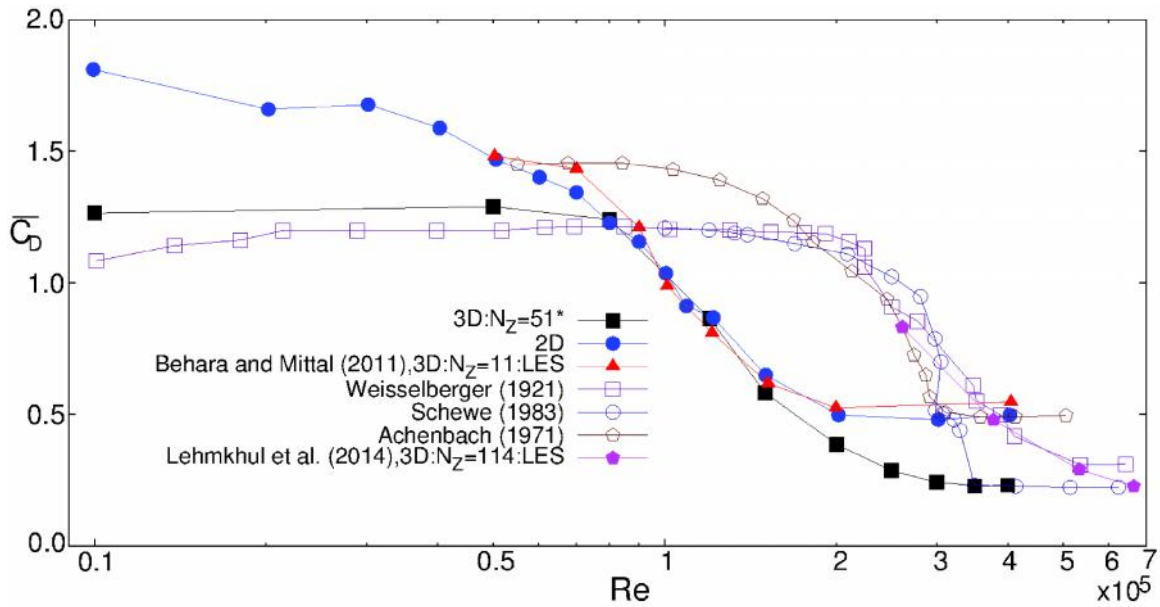


Fig. 2: Flow past a cylinder: Variation of the mean drag coefficient with Reynolds number

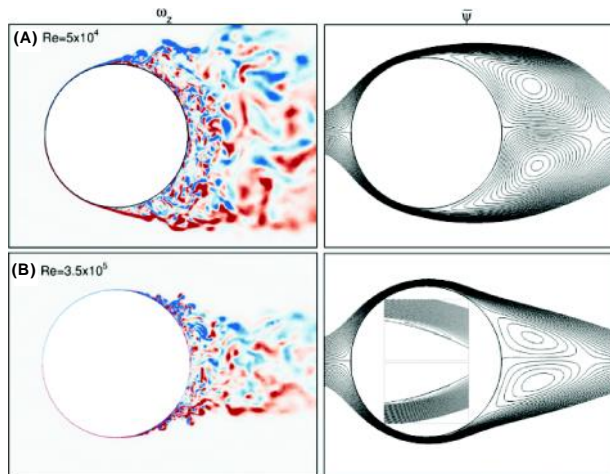


Fig. 3: Flow past a cylinder: instantaneous pictures of spanwise vorticity (left) and time and span averaged streamlines (right) at (A) $Re=5 \times 10^4$ and (B) $Re=3.5 \times 10^5$

Intermittency factor (I_f). This is a well-established concept in turbulence where, intermittency represents the fraction of time a flow is in turbulent state. In the present work I_f represents the fraction of time an LSB is present in the flow. The value of I_f lies between 0 and 1, where 0 indicates LSB never appears in the flow while a value of 1 corresponds to the LSB being present at all times in the flow. The Intermittency factor is estimated from the root mean square (rms) of fluctuations of the coefficient of pressure (C_p) on the surface of cylinder. Fig. 4 shows the distribution

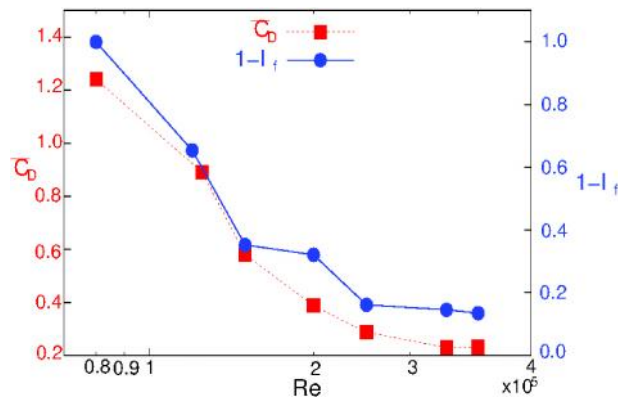


Fig. 4: Flow past a cylinder: variation of the intermency factor and mean coefficient of drag with Re

of $1-I_f$ and \bar{C}_D with Re. It can be observed from the figure that there is a very good correlation between $1-I_f$ and the mean coefficient of drag. In the subcritical regime, where the boundary layer undergoes laminar separation without reattachment, $1-I_f$ is one and the \bar{C}_D is high. The LSB is never formed in this flow. In the critical regime when the drag reduces with increase in Re, $1-I_f$ also reduces. In the lower critical regime, the LSB begins to appear in the flow but exhibits an intermittent nature. This is reflected in the relatively large value of $1-I_f$. On the other hand, towards the end of the drag crisis, $1-I_f$ approaches zero. This

indicates that LSB is present in the flow at all times. This analysis clearly shows that the drag crisis and transition of boundary layer from laminar to turbulent state is a relatively gradual process spanning across the critical regime. The LSB does not appear suddenly at a certain Re ; rather it appears intermittently with increased presence with increase in Re .

Vortex Induced Vibrations (VIV)

Unsteady aerodynamic forces resulting from vortex shedding in flow past bluff bodies may lead to its vibrations. If unattended, such vibrations may cause fatigue damage and in many cases lead to catastrophic failure of structures. Therefore, vortex-induced vibration (VIV) is considered as a problem of practical importance in several branches of engineering, e.g. oscillation of oil risers bringing oil from the sea bed. Recently, there has been surge in VIV studies because of its application in harvesting energy from the flow along the sea bed. The response of the structure undergoing free vibrations depends on many parameters. This research mainly focuses on exploring the effect of Re , shape and mass of the body, structural damping and natural frequency on VIV. An important phenomenon associated with VIV is *lock-in/synchronization/wake-capture*. During lock-in, the structure exhibits large amplitude of oscillation. In this regime, the frequency of vortex shedding is different from the situation when the structure is stationary. We investigate VIV for the flow past bodies with different geometries over a wide range of Re . 2D and 3D computations are carried out depending on the flow regime. It is observed that the peak amplitude of oscillation increases with increase in Re (Navrose and Mittal, 2011). For low values of Re , the response of a circular cylinder is associated with two branches: *initial and lower* (Fig. 5). At large Re , a third branch called the *upper* branch appears (Fig. 6). The different branches of cylinder response are associated with different modes of vortex shedding. Each mode is associated with different level of fluctuations in the lift forces. The transition between different branches may be associated with hysteresis or intermittent switching. In general, the upper branch is associated with the largest fluctuation in lift force as well as the peak amplitude of cylinder oscillation. To investigate the effect of proximity of another body on free vibrations of a cylinder, computations are carried out with multiple cylinders in different configurations. The

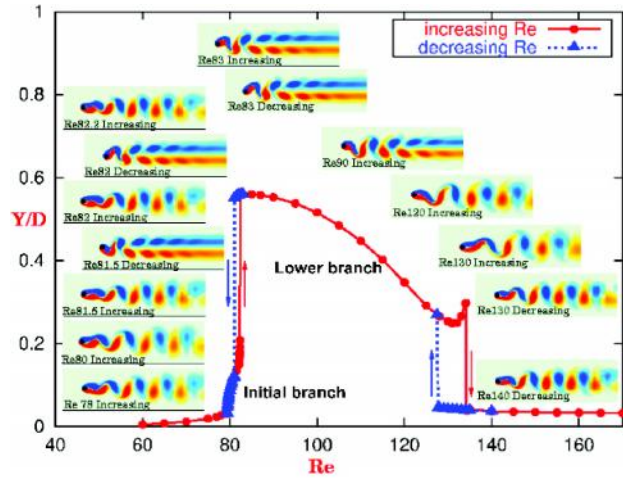


Fig. 5: Flow past a freely vibrating cylinder in low Re regime: the two branches of cylinder response and the mode of vortex shedding at different Re (Navrose and Mittal, 2011)

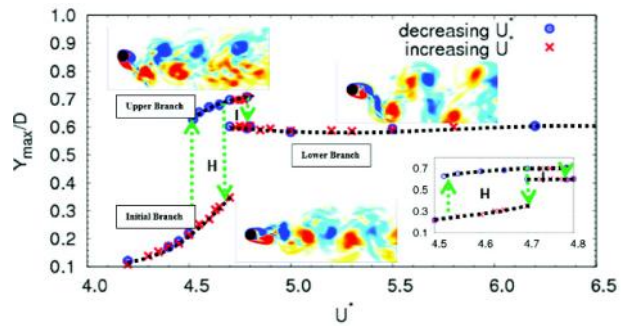


Fig. 6: Flow past a freely vibrating cylinder at $Re=1000$: the three branches of cylinder response and the different modes of vortex shedding on the different branches (Navrose and Mittal, 2011)

size of the cylinders and the spacing between them in found to have significant impact on the response of the cylinder and the wake. The effect of finite eccentricity on VIV is also explored. It is observed that an elliptic cylinder with minor axis aligned parallel to the incoming flow experiences larger amplitude of oscillation compared to the situation where the major axis is aligned parallel to the flow. The aspect ratio is also found to affect the width of the lock-in regime. The effect of imparting rotation to the body is also explored. Such VIV scenarios are quite important for off shore drilling processes. With increase in the rotational speed, the peak amplitude of circular cylinder increases, reaching a value that is several times the diameter of the cylinder. The range of large amplitude oscillation increases with increase in the

rate of rotation. Compared to its circular counterpart, VIV of square cylinder is found to be associated with higher amplitude of oscillation and richer vortex shedding patterns. Depending on the orientation of the square cylinder with respect to the incoming flow galloping oscillation can also occur alongside VIV.

Fluid Structure Interaction of Cylinder With Splitter Plate

Problems involving effect of fluid structure interaction (FSI) of flexible splitter plates on flow past circular and square cylinders are numerically studied. An open-source program, based on standard Galerkin discretization, Calculix, is employed for solving the structural dynamics equations. A block iteration based partitioned approach is utilized to couple the fluid and structure sub-problems.

Furquan and Mittal, 2014 studied the flow past two rigid square cylinders with attached flexible splitter plates, placed side-by-side in a uniform flow. The Re of the flow is fixed at 100, while the flexibility of the plates, Ae , is varied. Initially, the plates exhibit small amplitude vibrations which are almost 180° out-of-phase with each other. The flow is symmetric about the centerline at this stage. However, this changes with time. Beyond a certain time, the plates begin to oscillate in phase. The fully developed oscillations are associated with large amplitude when the frequency of plate oscillations is close to the natural frequency of the plates. Fig. 7 shows an instantaneous vorticity field for both in-phase and out-of-phase oscillations for the case with $Ae=8.05 \times 10^5$.

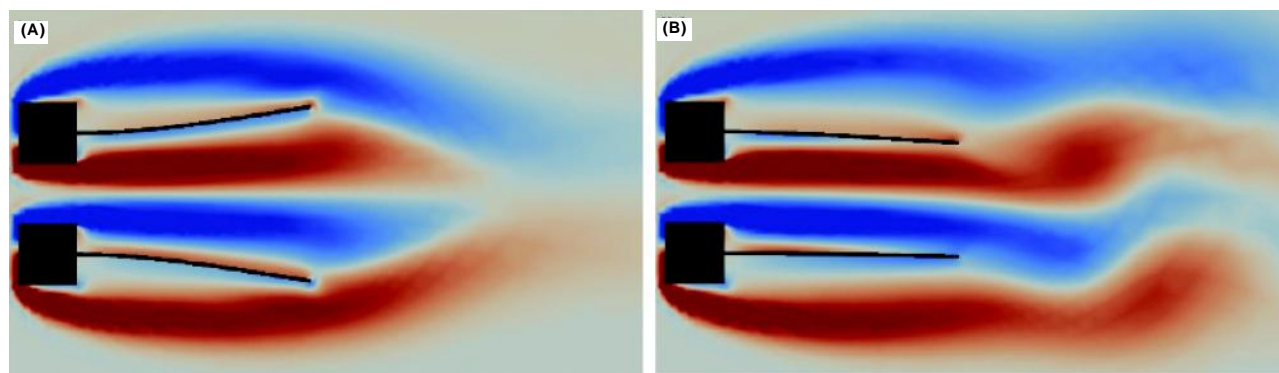


Fig. 7: Instantaneous vorticity field for flow past two side-by-side square cylinders with attached splitter plates for $Re=100$ and $Ae=8.05 \times 10^5$ showing (A) out-of-phase oscillations during the initial stage of the solution, (B) fully developed in-phase oscillations (Furquan and Mittal, 2014)

The effect of flexibility of the splitter plate on the vibration of an elastically mounted circular cylinder is studied at $Re=150$. When the splitter plate is relatively rigid, it is able to suppress the VIV of the cylinder. However, at large reduced speeds the galloping oscillations set in. The amplitude of oscillations is found to increase with increase in the reduced speed. Highly flexible plates, on the other hand, do not show galloping response but are less effective in controlling VIV of the cylinder. The study suggests that there exists an optimal value of flexibility to effectively control both VIV and galloping oscillations. Fig. 8 shows instantaneous vorticity field for the case of density ratio = 10, reduced velocity $U_s^*=6$ and $Ae=44571$.

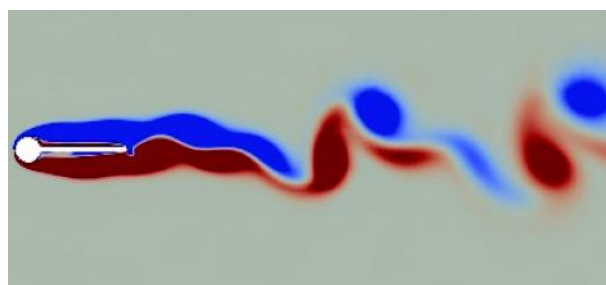


Fig. 8: Instantaneous vorticity field for flow past an elastically mounted cylinder with an attached flexible splitter plate. The figure shows instantaneous vorticity field for $Re=150$, density ratio = 10, $U_s^*=6$ and $Ae=44571$

Aerodynamic Shape Optimization in Fluid Flows using Adjoint Approach

Shape optimization in fluid mechanics is on its way to becoming an integral part of the design process. Srinath and Mittal, 2010 formulated and implemented a

continuous adjoint-based method for shape optimization in steady low Re flows. This method was utilized to design optimal airfoils at low Re. Adjoint methods are most effective in optimization as the cost of computing the gradients or sensitivities are independent of the number of design variables (Kumar *et al.*, 2013). The shape of the body is parametrized via a Non-Uniform Rational B-Splines (NURBS) curve and is updated by using the gradients obtained from solving the flow and adjoint equations. The adjoint equations are also solved using SUPG and PSPG methods. The L-BFGS algorithm is employed to minimize the objective function and provide a new search direction depending on the gradients. Shape optimization was extended to unsteady flows by Srinath and Mittal, 2010 for airfoil at $Re = 10,000$. Interesting shapes are obtained with NACA 0012 as initial guess, especially when the objective is to produce high performance airfoils. Fig. 9(A) shows the airfoil obtained for an inverse coefficient of lift = 0.75 and (B) coefficient of pressure distribution for $Re = 1000$ flow at $\alpha = 4^\circ$. There is an increase in lift of 275 % compared to the initial guess.

The effect of corrugations on the aerodynamic performance of a Mueller C4 airfoil, placed at a 5° angle of attack, at $Re=10,000$ was investigated by Sambhav *et al.*, 2015. The computations were carried out for different location and number (n) of corrugations while keeping the height of the corrugation ($h=1.5\%c$) fixed. PTOC (Preserve thickness, optimize camber) optimization strategy was used to obtain the highest lift coefficient and aerodynamic efficiency of 0.997 and 16.9, respectively. This is 42 % and 7% higher than Mueller C4 airfoil. The optimal shape is shown in Fig. 10(B).

Elliptic and rectangular planforms were

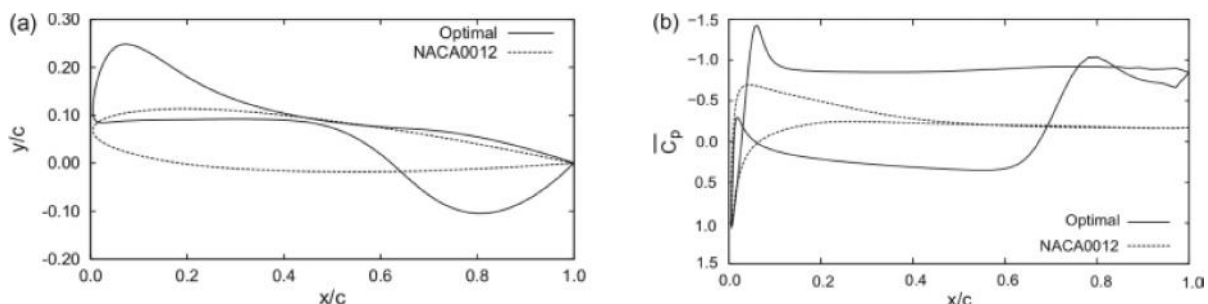


Fig. 9: Inverse design of airfoil for coefficient of lift = 0:75 at $Re = 1000$, $\alpha = 4^\circ$: (a) initial and optimal shapes and (b) time-averaged coefficient of pressure distribution on surface (Srinath and Mittal, 2010)

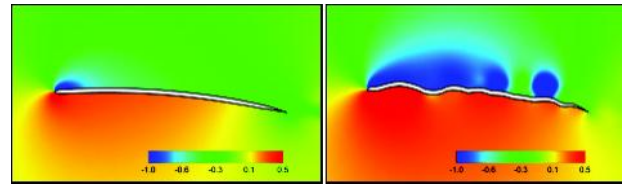


Fig. 10: Pressure distribution for flow past (A) Mueller C4 airfoil and (B) Optimal airfoil obtained through PTOC strategy (Sambhav *et al.*, 2015)

optimized for $Re=1000$ based on root chord and $\alpha = 4^\circ$ to the oncoming flow by Kumar *et al.*, 2013. A 3D wing is parametrized by a control net, obtained by stacking control polygons at different of spanwise locations. Biparametric tensorial NURBS surface is interpolated on the control net to generate the wing surface. Fig. 11 shows the control net and the resulting NURBS surface for a wing with elliptic planform. Fig. 12 shows the comparison of planform shapes and Fig. 13 shows iso-surface of the streamwise component of vorticity ($\omega_x = -0.3$) for all the planforms. The length of the wing-tip vortex is longer for the rectangular and elliptic planform whereas it is shorter for the optimal shape with an additional weak vortex at the winglet type structure near the wing-tip. The optimal shape has 15 % increase in aerodynamic efficiency compared to the other planforms.

Supersonic Flow in Air Intakes

The purpose of an air-intake is to capture free-stream air and bring it to an optimal condition desired by engine. In the case of a supersonic aircraft, this is achieved by a design that slows the flow via a train of oblique shock waves, followed by a weak normal shock. In this study, Y-intake and mixed compression air intakes are considered. Flow in Y-intake configuration was studied by Kotteda and Mittal, 2015.

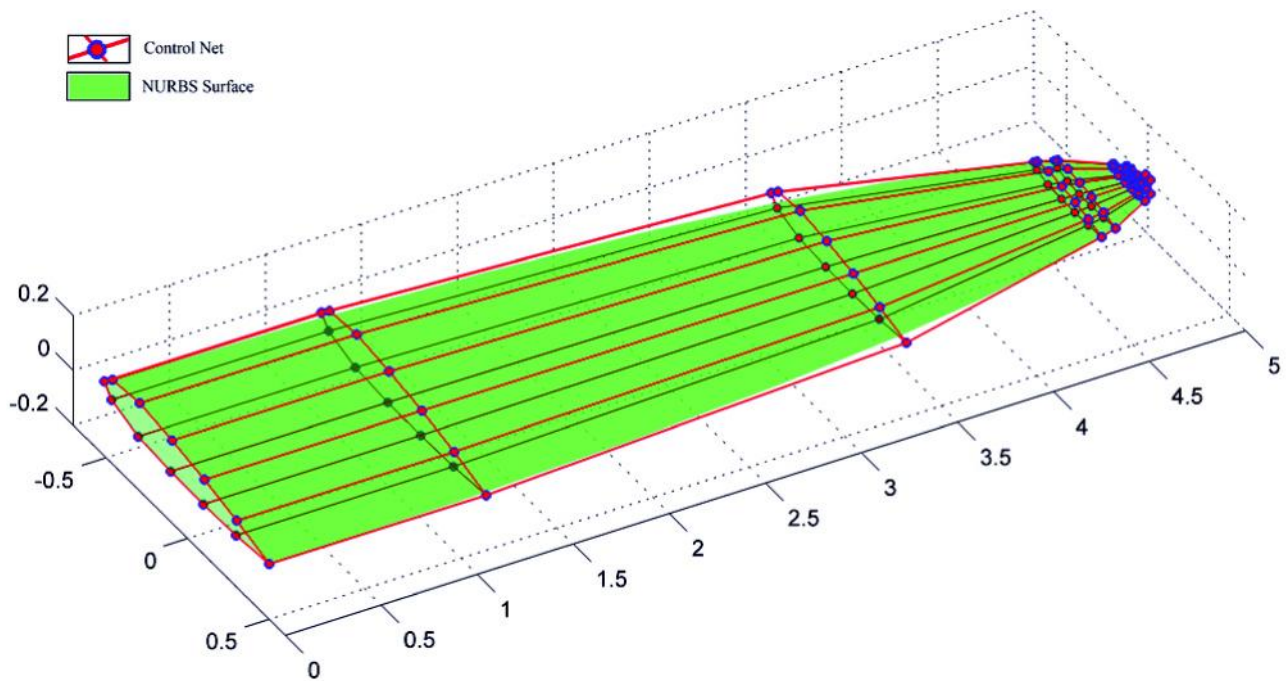


Fig. 11: Representation of an elliptic wing at $\alpha = 4^\circ$ with a NURBS surface (Bhatt *et al.*, 2015)

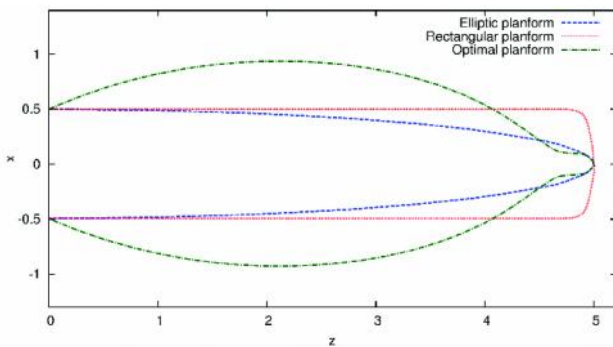


Fig. 12: Comparison of planforms shapes for $Re = 1000$ flow at $\alpha = 4^\circ$ (Bhatt *et al.*, 2015)

The Y-intake configuration is used in many modern supersonic fighter aircrafts with single engine which have high manoeuvrability. The computations are carried out at $M=1.5$ with different back pressure ratios (p_b/p_i) and sideslip angles (β). The performance of the intake is studied for $2.1 < p_b/p_i < 3.5$ and $0^\circ < \beta < 5^\circ$. The onset of buzz instability in the intake is observed at $p_b/p_i = 3.276$ for $\beta=3^\circ$. It is shown in Fig. 14. The first three frames show a buzz cycle. In the first and last flow frames, the bow shocks are at their most downstream locations while they are at their

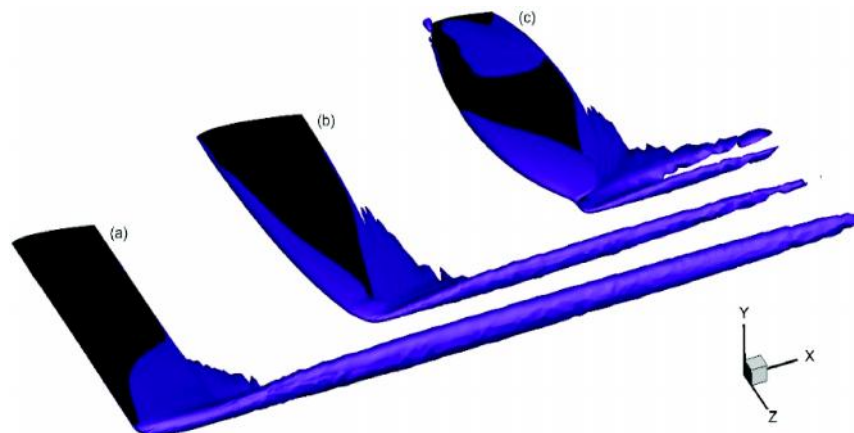


Fig. 13: Comparison of iso-surfaces of streamwise vorticity for (a) rectangular, (b) Elliptical, and (c) optimal planform for $Re=1000$ flow at $\alpha = 4^\circ$ (Bhatt *et al.*, 2015)

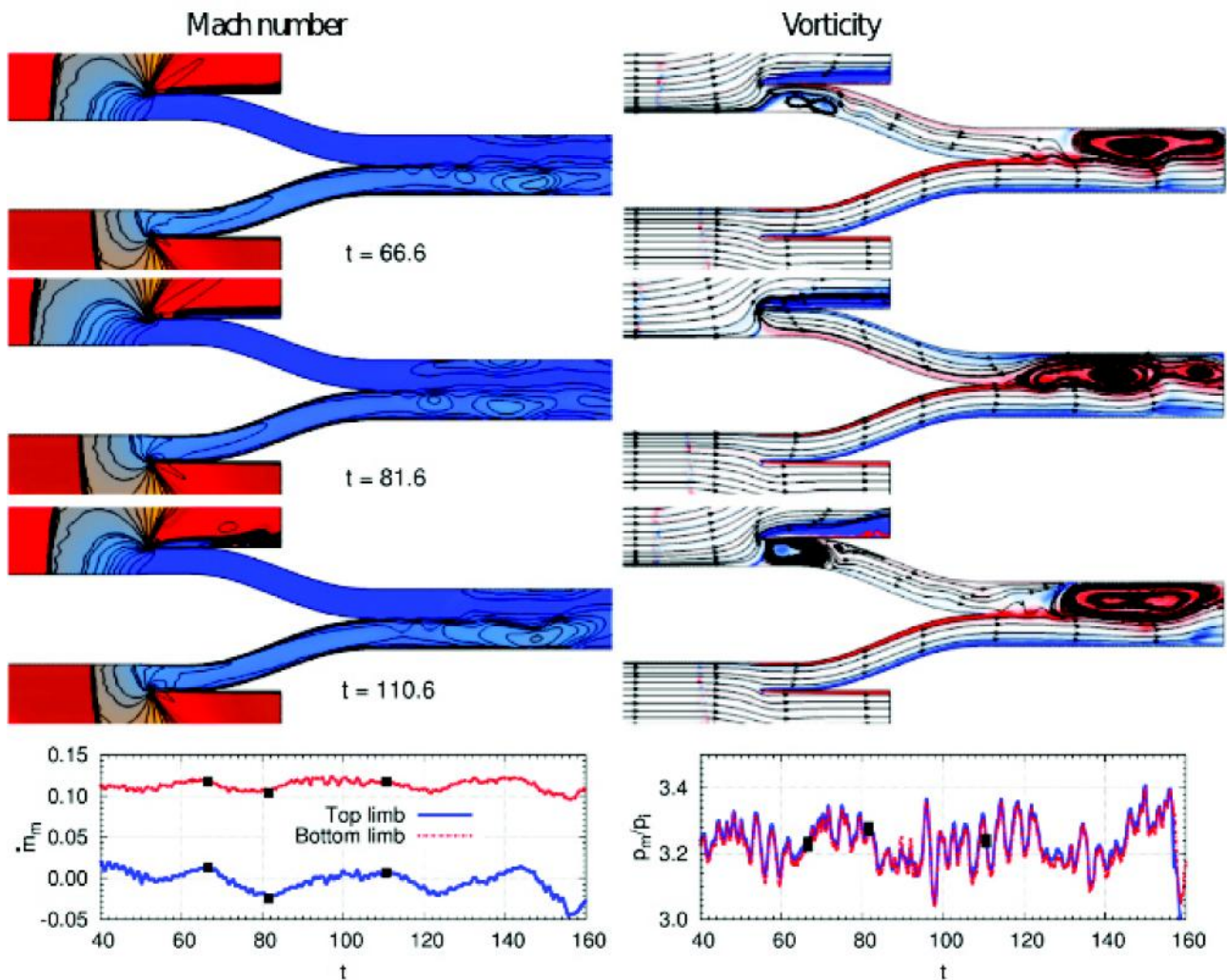


Fig. 14: $M=1.5$, $Re=1 \times 10^5$, $\alpha = 3^\circ$, $p_b/p_i = 3.276$ flow in the Y-intake at various time instants during onset of instability. Time histories of the mass flow rate in the top and bottom limb (left) and pressure at the middle of the top and bottom limb (right) at the merger section are shown in the last row. The time instants at which the flow is shown are marked on these plots (Kotteda and Mittal, 2015)

most upstream location in the second frame. The net flow in the bottom limb is always positive. However, the top limb experiences a reverse flow during part of the buzz cycle as also seen in the time history of the mass flow rate. Streamlines as well as vorticity fields are shown in the right column of Fig. 14. The upstream movement of the bow shock can be seen in second frame. It is accompanied with an upstream movement of the vortex, located in the duct beyond the merger section, and the reverse flow in the top limb. The negative mass flow rate in the top limb corresponding to the second frame can be seen in the time history. The bow shocks upstream of the top and bottom limbs move back and forth leading to very

large amplitude oscillations in the mass flow rate delivered to the engine face. The buzz cycle is fairly periodic and repeats itself. Interestingly, the net mass flow rate through the intake is still positive and the engine continues to receive air flow, but at a reduced level.

Cellular Oblique Vortex Shedding

It is well known that due to the end wall effects, the vortex shedding past a cylinder is associated with vortices oblique to the axis of the cylinder. Another feature due to the presence of the walls is the formation of a cellular structure of the vortices along the span. The present work focuses on the analysis

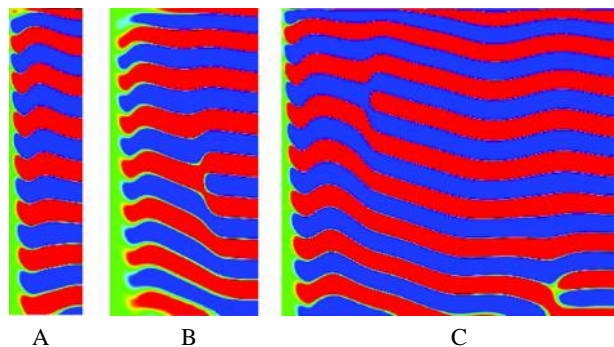


Fig. 15: Flow past a three dimensional cylinder with end walls: instantaneous spanwise vorticity for (A) one-cell, (B) two-cell and (C) three cell shedding patterns

of flow past a 3D circular cylinder at low Re in the laminar flow regime. Three key parameters have been identified that characterize the flow - Aspect Ratio (AR) of the cylinder, Re and boundary condition at the cylinder ends. The aim of the study is to characterize the flow in the parameter space of AR and Re , and attempt to understand the reasons that lead to cellular shedding. In this study, numerical simulations have been carried out to simulate flow past a wall bounded finite cylinder to study the effect of each parameter. Computations have been carried out for $10 < AR < 150$ and $50 < Re < 100$. The effect of end conditions is studied by varying the length of the

end-plate so that the thickness of the boundary layer can be controlled. The flow is broadly classified based on the number of spanwise cells, the type of dislocations and the spatio-temporal variation of the oblique angle of the vortices. It is found that the dislocations appear periodically in time. Beyond a certain AR, the flow is unsteady. The number of spanwise cells in the flow ranges between one and three. There are notable differences in shedding patterns across $Re \sim 64$. For $Re < 63$, the flow is relatively complex and shows spatio-temporal variations in the oblique angle of the vortices. On the other hand, only spatial variations are observed for $Re > 65$. The vortex structures in one-cell, two-cell, and three-cell patterns are shown in Fig. 15.

Conclusions

Several fundamental and interdisciplinary problems have been attempted using stabilized finite element method. The simulations help in explaining the underlying complex flow physics.

Acknowledgement

Authors would like to acknowledge present and past members of Computational fluid dynamics group at IIT, Kanpur for carrying out the research work presented in this paper.

References

- Achenbach E (1968) Distribution of local pressure and skin friction around a circular cylinder in cross-flow up to $Re=5 \times 10^6$ *J Fluids Mech* **34** 625-639
- Behara S and Mittal S (2009) Parallel finite element computation of incompressible flows *Parallel Computing* **35** 195-212
- Behara S and Mittal S (2011) Transition of the boundary layer on a circular cylinder in the presence of a trip *J Fluids Struct* **27** 702-715
- Bhatt V D, Srinath D N and Mittal S (2015) Aerodynamic shape optimization using stabilized finite element method *Math Models Methods Appl Sci* **25** 19-23
- Furquan M and Mittal S (2014) Flow past two square cylinders with flexible splitter plates *Comput Mech* **55** 1-12
- Kotteda V M K and Mittal S (2015) Flow in a Y-Intake at supersonic speeds *J Propulsion Power* 1-17
- Kotteda V M K and Mittal S (2011) Viscous flow in mixed compression intake *Int J Numer Methods Fluids* **67** 1393-1417
- Kumar N, Diwakar A, Attree S K and Mittal S (2013) A method to carry out shape optimization with a large number of design variables *Int J Numer Methods Fluids* **71** 1494-1508
- Lehmkuhl O, Rodríguez I, Borrell R, Chiva J and Oliva A (2014) Unsteady forces on a circular cylinder at critical Reynolds numbers *Phys Fluids* **26** 110-125
- Navrose and Mittal S (2013) Free vibrations of a cylinder: 3-D computations at $Re=1000$ *J Fluids Struct* **41** 109-1180
- Prasanth T K and Mittal S (2008) Free v/s forced vibrations of a cylinder at low Re *Int J Comput Fluids Dynamics* **22** 583-592
- Rosko A (1961) Experiments on the flow past a circular cylinder at very high Reynolds number *J Fluids Mech* **10** 345-356
- Saad Y and Schultz M H 1986 GMRES: A generalized minimal residual algorithm for solving non-symmetrical linear

- systems *SIAM J Scientific and Statistical Computing* **7** 856-869
- Sambhav J, Bhatt V D and Mittal S (2015) Shape optimization of corrugated airfoils *Comput Mech* **56** 917-930
- Schewe G (1983) On the force fluctuations acting on a circular cylinder in crossflow from subcritical up to transcritical Reynolds numbers *J Fluids Mech* **133** 265-285
- Schlichting H and Gersten K (2004) *Boundary Layer Theory* Springer New York
- Singh S P and Mittal S (2005) Flow past a cylinder: Shear layer instability and drag crisis *Int J Numer Methods Fluids* **47** 75-98
- Srinath D N and Mittal S (2007) A stabilized finite element method for shape optimization in low Reynolds number flows *Int J Numer Methods Fluids* **54** 1451-147
- Srinath D N and Mittal S (2010) An adjoint method for shape optimization in unsteady viscous flows *J Comput Physics* **229** 1994-2008
- Tezduyar T E, Mittal S, Ray S and Shih R (1992) Incompressible flow computations with stabilized bilinear and linear equal-order-interpolation velocity-pressure elements *Computer methods in Applied Mechanics and Engineering* **95** 221-242.